Magnetic resonance fingerprinting for simultaneous renal T_1 and T2* mapping in a single breath-hold

Hermann, Ingo; Chacon-Caldera, Jorge; Brumer, Iréne; Rieger, Benedikt; Weingärtner, Sebastian; Schad, Lothar R.; Zöllner, Frank G.

DOI
10.1002/mrm.28160

Publication date
2020

Document Version
Final published version

Published in
Magnetic Resonance in Medicine

Citation (APA)
Hermann, I., Chacon-Caldera, J., Brumer, I., Rieger, B., Weingärtner, S., Schad, L. R., & Zöllner, F. G. (2020). Magnetic resonance fingerprinting for simultaneous renal T_1 and T2* mapping in a single breath-hold. *Magnetic Resonance in Medicine*, *83*(6), 1940-1948. https://doi.org/10.1002/mrm.28160

Received: 16 September 2019 | Revised: 11 December 2019 | Accepted: 11 December 2019

DOI: 10.1002/mrm.28160

RAPID COMMUNICATION

Magnetic Resonance in Medicine

Magnetic resonance fingerprinting for simultaneous renal T_1 and T_2^* mapping in a single breath-hold

Ingo Hermann[1,2] | **Jorge Chacon-Caldera**[1] | **Iréne Brumer**[1] | **Benedikt Rieger**[1] | **Sebastian Weingärtner**[2] | **Lothar R. Schad**[1] | **Frank G. Zöllner**[1]

[1]Computer Assisted Clinical Medicine, Medical Faculty Mannheim, Heidelberg University, Mannheim, Germany

[2]Magnetic Resonance Systems Lab, Department of Imaging Physics, Delft University of Technology, Delft, Netherlands

Correspondence
Ingo Hermann, Computer Assisted Clinical Medicine, Medical Faculty Mannheim, Heidelberg University, Theodor.Kutzer-Ufer 1-3, 68167, Mannheim, Germany.
Email: ingo.hermann@medma.uni-heidelberg.de

Purpose: To evaluate the use of magnetic resonance fingerprinting (MRF) for simultaneous quantification of T_1 and T_2^* in a single breath-hold in the kidneys.

Methods: The proposed kidney MRF sequence was based on MRF echo-planar imaging. Thirty-five measurements per slice and overall 4 slices were measured in 15.4 seconds. Group matching was performed for in-line quantification of T_1 and T_2^*. Images were acquired in a phantom and 8 healthy volunteers in coronal orientation. To evaluate our approach, region of interests were drawn in the kidneys to calculate mean values and standard deviations of the T_1 and T_2^* times. Precision was calculated across multiple repeated MRF scans. Gaussian filtering is applied on baseline images to improve SNR and match stability.

Results: T_1 and T_2^* times acquired with MRF in the phantom showed good agreement with reference measurements and conventional mapping methods with deviations of less than 5% for T_1 and less than 10% for T_2^*. Baseline images in vivo were free of artifacts and relaxation times yielded good agreement with conventional methods and literature (deviation T_1: $7 \pm 4\%$, T_2^*: $6 \pm 3\%$).

Conclusions: In this feasibility study, the proposed renal MRF sequence resulted in accurate T_1 and T_2^* quantification in a single breath-hold.

KEYWORDS

T_1 mapping, T_2^* mapping, magnetic resonance fingerprinting, quantitative kidney imaging

1 | INTRODUCTION

Magnetic resonance fingerprinting (MRF) is a promising method to quantify multiple tissue properties in a single, time-efficient acquisition. Imaging of the relaxation times T_1, T_2, T_2^* has been achieved simultaneously with different acquisition and readout schemes. Its application is increasingly gaining clinical relevance.[1-7] In MRF, unique fingerprints are generated by a pseudo-random pulse design with varying flip angles, echo (TE), and repetition times (TR) to generate

---

different sets of contrast weightings. These are matched with precomputed dictionaries containing all relevant combinations of physiological tissue parameters.

The original MRF sequence was based on a steady-state free precession (SSFP) readout with highly undersampled spiral k-space readout and remains the most commonly used approach. Recently, an alternative MRF acquisition was proposed based on a Cartesian echo-planar imaging readout.[8] Compared to conventional MRF, MRF echo-planar imaging (MRF-EPI) affords increased robustness against system imperfections at the trade-off against a reduced number of baseline images. Furthermore, interpretable baseline images in MRF-EPI allow monitoring for patient specific artifacts or motion during the acquisition and facilitates clinical robustness. In-line reconstruction on the scanner with a fast group matching algorithm[9] allows the integration into clinical workflow.

MRF has become a widely available for neuroimaging but application to abdominal imaging is limited.[10] Especially MRF is rarely used for renal imaging.

Chronic kidney disease affects around 10% of the world population and is induced by pathological changes such as inflammation, fibrosis, and edema. These process were shown to increase T_1[11] and, hence, quantitative renal imaging is clinically relevant for detecting a spectrum of pathologies.[12-15] Changes in oxygen supply can be visualized in the blood oxygenation level-dependent effect, which correlates with T_2^*, and has been observed to decrease in CKD and kidney transplants.[16-19]

The most commonly used method for renal T_1 mapping is the modified Look-Locker inversion recovery (MOLLI),[11,20,21] which is based on an inversion recovery pulse followed by several imaging readouts. However, the repeated imaging acquisitions disturb the longitudinal magnetization recovery and compromise acquisition accuracy.[22] The gold standard technique for T_2^* quantification is multiple gradient echo (multi-GRE).[23-25]

Conventional MRI scans suffer from long acquisition times. Ding et al have previously demonstrated the clinical value of simultaneous T_1 and T_2^* estimation.[26] Their technique was based on EPI readout with inversion recovery (IR) preparation for T_1 and a saturation pulse followed by multiple GRE acquisitions for T_2^* quantification. Nevertheless, the low resolution and the long acquisition time for one slice is outperformed by MOLLI and multi-GRE. Especially, measuring multiple slices in multiple breath-holds increases the measurement time substantially as 10-30 seconds pauses are required between breath-holds. However, MOLLI underestimates the T_1 times as well-known from factors such as magnetization transfer[27] and multi-GRE measurements may overestimate T_2^* for long echo times at 3T.[28]

In this study, we aim to implement a MRF sequence based on an EPI readout to estimate T_1 and T_2^* times in the entire kidneys in a single breath-hold. Phantom measurements are performed to validate the accuracy and precision of the T_1 and T_2^* quantification for 4 slices and to optimize scan-time efficiency. Whole kidney in vivo MRF maps are acquired and compared to the gold standard methods MOLLI and multi-GRE to study the feasibility.

2 | METHODS

2.1 | Sequence parameters

All measurements were performed on a 3T MRI scanner (Magnetom Skyra; Siemens Heathineers, Erlangen, Germany) with a 28-channel receiver coil array and shared the following common imaging parameters: FOV = $380 \times 380\,\text{mm}^2$, matrix size (base resolution) = 256 × 256 ($1.5 \times 1.5\,\text{mm}^2$), slice thickness = 5 mm. The proposed MRF method was based on[8] with the following specific parameters: bandwidth = 1148 Hz/px, GRAPPA-factor 3 with 36 calibration lines, partial Fourier 5/8, fat saturation, and varying flip angle α (17-43°), TE (16-76.5 ms), TR (383-625 ms) as shown in Figure 1. TE and TR are depicted as the same line (gray) because they are proportional to each other, only minimal and maximal values are different. Additionally, T_1 maps were generated using a 5(3s)3 MOLLI[29] scheme with the same common parameters and bandwidth = 1085 Hz/px, GRAPPA-factor 2, partial Fourier 6/8, and flip angle 35°. T_2^* maps were generated using a multi-GRE sequence with the same common parameter and bandwidth = 390 Hz/px, GRAPPA-factor 2, partial Fourier 6/8, and flip angle 18° with 12 different TEs varying from 1.7-40 ms.

2.2 | Dictionary

The dictionaries were generated by Bloch simulations off-line using MATLAB (The MathWorks; Natick, Massachusetts). The evolution of the magnetization was simulated with B_1^+ compensation by a scaling factor for the excitation flip angles[2] and pattern matching is performed using the magnitude data. A group matching algorithm was implemented based on the method by Cauley et al[30] where the full dictionary is divided into multiple small dictionaries. The mean value of all small dictionaries is written in an additional look up table (LUT). The measured signal is matched with the LUT containing the mean values and the best matching groups are chosen to fully correlate with the measured signal. The best matching groups were precomputed by correlating the LUT containing the mean values with itself and sorted by the correlation values. For every group, the sorted best matching groups were written in an additional LUT. The full dictionary was splitted into 4682 smaller dictionaries (groups)

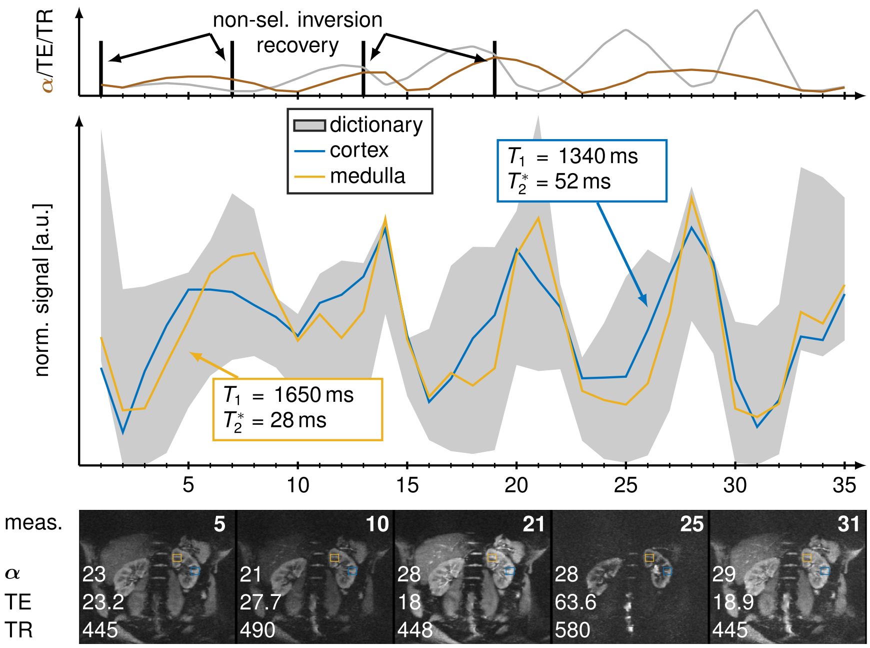

FIGURE 1 Evolution of the measured signal for all 35 measurements. On top, the varying α (17-43°), TE (16-76.5 ms), TR (383-625 ms), and the inversion pulses are depicted. TE and TR are depicted as the same line because their trend is proportional (TR = 4·TE+const.) and just minimal and maximal values differ. The evolution curve of the renal cortex (blue) and the renal medulla (yellow) is shown with its corresponding T_1 and T_2^* times for one exemplary measurement. All entries of the full dictionary are depicted as gray area. Baseline images on the bottom show different weightings for several α, TE, and TR along the evolution curve

containing 15 entries each. 200 of these groups were used to match the pixelwise signal which were preselected by the LUT containing the mean of every group. The full dictionaries consisted of 70,236 entries with T_1 ranging from 100 to 3500 ms, T_2^* from 10 to 2000 ms with increasing step size and flip angle efficiency (B_1^+) from 0.7 to 1.2 with a step size of 0.1. All entries with $T_1 < T_2^*$ were discarded. The calculation of the dictionary took less than 10 minutes. Parameter maps were reconstructed in-line on the scanner.[9] Inversion pulses were assumed to be ideal (180°) with no T_2^* decay during the pulse. Multi-threading was used to simultaneously match multiple slices at the same time for efficient postprocessing.

2.3 | Phantom experiments

Phantom measurements were performed to evaluate accuracy and precision of the MRF sequence compared to references measurements. Inversion-recovery turbo spin echo was performed for T_1 quantification with TI = 100, 200, 500, 1000, 2000, 3000, 5000, 10000 ms, TE/TR = 12/10000 ms, turbo factor = 16, FOV = 320 × 320 mm^2, matrix size (base resolution) = 256 × 256 (1.3 × 1.3 mm^2), slice thickness = 5 mm, bandwidth = 1085 Hz/px. Multi-GRE was performed for T_2^* quantification with 28 contrasts within TE = 2-50 ms, FOV = 320 × 320 mm^2, matrix size (base resolution) = 256 × 256 (1.3 × 1.3 mm), slice thickness = 5 mm, bandwidth = 390 Hz/px. MRF was performed with the common sequence parameters. In total, 100 baseline images with different contrast weighting were acquired to calculate the parameter maps yielded by an increasing amount of measurements to study the convergence of the parametric maps. Hereby, the scheme of varying flip angles, TE and TR is repeated after every 35 measurements. The MRF maps were acquired 10 times for studying precision and reproducibility compared to MOLLI and multi-GRE and reference IR and GRE. Precision was calculated by taking the standard deviation of the difference of every measurement to their mean. The phantom consisting of tubes was generated using 12 different mixtures of water, agarose and NiCl$_2$ as recommended by Captur et al.[31] The whole phantom was submerged in water to reduce susceptibility artifacts.

2.4 | In vivo experiments

In vivo measurements were performed in 8 healthy volunteers (6 male, 22-33 years old) to study the feasibility compared to commonly used methods as MOLLI for T_1 and multi-GRE for T_2^* quantification. All breath-holds were performed in end-expiration. MRF, MOLLI, and multi-GRE were performed using the parameters as described in the previous section. Coronal slices were chosen as imaging planes.

Medulla and cortex were semi-automatically segmented using MATLAB (The MathWorks; Natick, Massachusetts). T_1 and T_2^* mean and standard deviations were calculated for all slices in the medulla and cortex, and all MRF measurements were registered using a 2D affine transformation using MATLAB (The MathWorks; Natick, Massachusetts). Ten MRF scans were performed to analyze precision of the measurements. Gaussian smoothing was performed on MRF baseline images to improve the matching process and therefore the parameter map quality. The Gaussian filter was implemented in-line on the scanner before the group matching. For this, the magnitude images were convolved with a Gaussian filter $G(i, j)$ with kernel size $n = 5$ as follows:

$$G_{i,j} = \frac{1}{2\pi\sigma^2}\cdot\exp\left(-\frac{i^2+j^2}{2\sigma^2}\right) \tag{1}$$

and the convolution in image space

$$I^*(x,y) = \sum_{i=1}^{n}\sum_{j=1}^{n} I\left(x-i+\frac{n-1}{2}, y-j+\frac{n-1}{2}\right) G(i,j) \tag{2}$$

with I^* the filtered pixel, I the image pixel, σ^2 the variance.

3 | RESULTS

3.1 | Phantom

Figure 2 shows the evolution of the matched T_1 and T_2^* times for the match process with an increasing amount of measurements for 3 different tubes. More than 20 measurements were needed for convergence of T_1 and T_2^*. Thus, 35 measurements were used as a standard for the MRF acquisition. Deviations in T_1 and T_2^* times of less than 5% and 10% were achieved which are comparable to MOLLI and multi-GRE. Standard deviations for T_2^* were lower than for multi-GRE. Scan time was reduced by a factor of 8 for the 4 slices compared to MOLLI and multi-GRE (8 measurements) considering 1 MRF acquisition providing both parameter maps with similar accuracy and precision in a phantom. Figure 3 depicts the T_1 and T_2^* map for MRF, MOLLI/multi-GRE and the reference IR and GRE of one representative slice.

Figure 4 shows in the top panel (A,C) the measured T_1 plotted against the reference T_1 for MRF (blue) and MOLLI (yellow) in (A), and the measured T_2^* for MRF (blue) and multi-GRE (orange) to the reference T_2^* in (C). Reference IR and GRE are depicted as a black line and the gray area

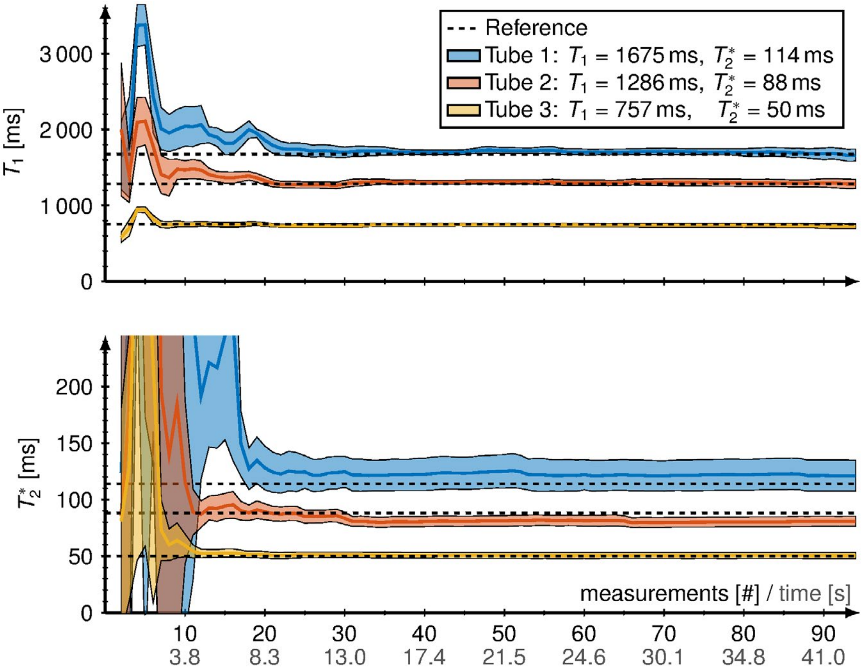

FIGURE 2 Convergence of the matched T_1 and T_2^* parameters for increasing measurements. Three different tubes are depicted with high (blue), medium (orange), and small (yellow) T_1 and T_2^* values. For more than 20 measurements, the matching converges to the reference value. The colored shaded areas show the standard deviations of the corresponding matched relaxation times

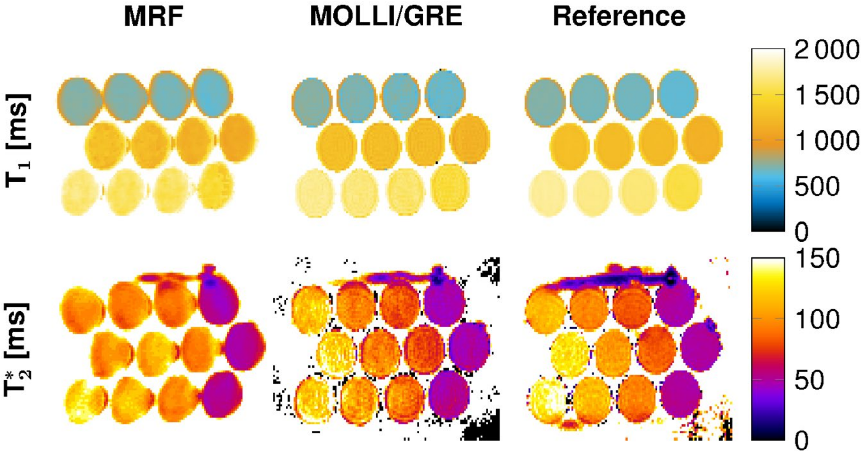

FIGURE 3 Representative quantitative T_1 (top) and T_2^* (bottom) maps in the phantom with 12 tubes. MRF on the left side, MOLLI/multi-GRE in the middle, and the reference IR and GRE on the right side

FIGURE 4 Comparison of T_1 on the left side (A) and T_2^* on the right side (C) between MRF (blue) compared to reference (black), MOLLI (yellow), and multi-GRE (orange). The gray area limits 5% deviation to the reference. The bottom panel shows the Bland-Altman plot for T_1 (B) and T_2^* (D). The difference from MRF, MOLLI, and multi-GRE to the reference methods is shown with the corresponding standard deviations. The gray line limits the area of 2 standard deviations

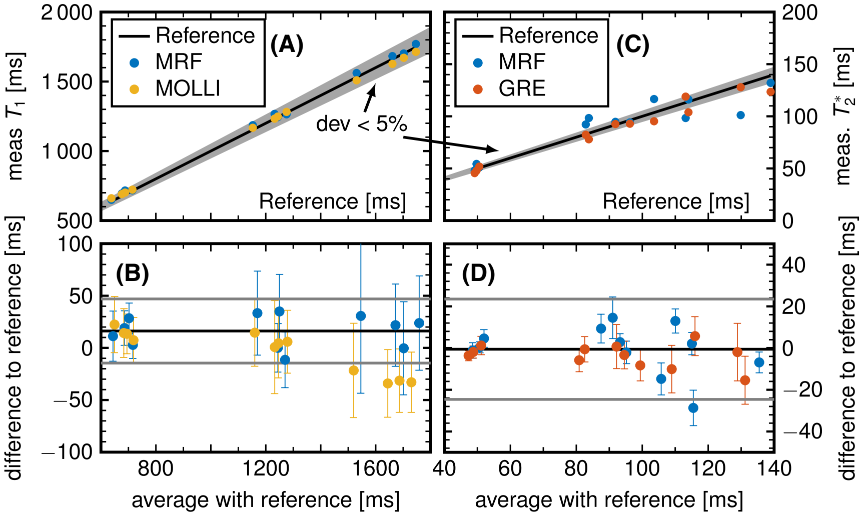

illustrates 5% deviation to the reference. MRF T_1 times show less than 5% deviation compared to the reference. T_2^* deviations vary between 4% and 10%. The corresponding Bland-Altman plots are shown in the bottom panel (B,D). MRF yields higher standard deviations than MOLLI between 25 ms for small T_1 and up to 75 ms for higher T_1 times, whereas MOLLI has standard deviations less than 40 ms for all T_1 times. On the right panel (D), MRF T_2^* times show smaller deviations than multi-GRE with maximum standard deviations of less than 10 ms, whereas multi-GRE shows standard deviations up to 15 ms.

Reproducibility and precision was evaluated by measuring the MRF sequence 10 times. Interscan variability for T_1 was less than 10 ms and for T_2^* less than 1.5 ms for all slices.

3.2 | In vivo

Figure 5 shows representative T_1 and T_2^* maps of 4 slices for one volunteer compared to the reference MOLLI and multi-GRE in coronal slice. Standard deviations of the T_2^* maps were similar compared to multi-GRE but MRF showed consistent higher T_2^* values. Mean MRF T_2^* times were 35.2 ms ± 5.6 ms and multi-GRE times were 30.3 ms ± 6.4 ms in the medulla and 54.7 ms ± 7.8 ms and 50.4 ms ± 7.2 ms in the cortex.

MRF T_1 times showed higher standard deviations and similar mean values compared to MOLLI. In the medulla, mean MRF T_1 times were 1921 ms ± 182 ms and for MOLLI 1950 ms ± 146 ms, and in the cortex, mean MRF T_1 times were 1456 ms ± 126 ms and for MOLLI 1432 ms ± 81 ms.

In vivo precision of T_1 acquired with MRF was 31 ms in the medulla and 65 ms in the cortex. Precision of T_2^* in the medulla was 1.4 ms and 1.8 ms in the cortex.

Ghosting artifact were alleviated using large FOV acquisitions and scan time was 15.4 seconds within one breath-hold. Online reconstruction on the scanner took less than 30 seconds.

Figure 6 shows the influence of Gaussian filtering on the correlation value, T_1 and T_2^* maps. As an example, a subject with noisy baseline images is shown. A fair compromise between sharp contours and edges and reduction of noise was obtained for $\sigma = 0.7$ which is shown in Figure 7 where the correlation value, T_1 and T_2^* with respect to the variance of the smoothing filter are depicted. The correlation values in the cortex were greater than 0.99 for $\sigma = 0.7$ and greater than 0.97 for $\sigma = 0$. On the bottom panel, the corresponding correlation value, T_1 and T_2^* is depicted over the variance for the cortex (blue) and the medulla (yellow). The standard deviation decreases for increasing variance of the Gaussian filter without changing the mean value of T_1 and T_2^*.

4 | DISCUSSION

This study demonstrates the feasibility of using an EPI-based MRF method to quantify the T_1 and T_2^* times in the kidneys covering 4 slices within one breath-hold. In phantom, good accuracy and precision was achieved with standard deviations comparable to MOLLI and multi-GRE as shown in previous publications.[8] MRF yielded accurate results for all T_1 times, whereas MOLLI lacks accuracy for long T_1 times due to magnetization transfer.[27] Fast and stable convergence of the parameter maps were achieved for increasing number of measurements. MRF using 35 measurements was a good compromise between scan time and parameter map quality. The shapes of the tubes were distorted by the EPI echo train due to inhomogeneities in B_0 and eddy currents, which induce inaccuracies in gradient amplitudes.[32,33]

In vivo scans yielded reproducible and accurate parameter maps comparable with MOLLI and multi-GRE with

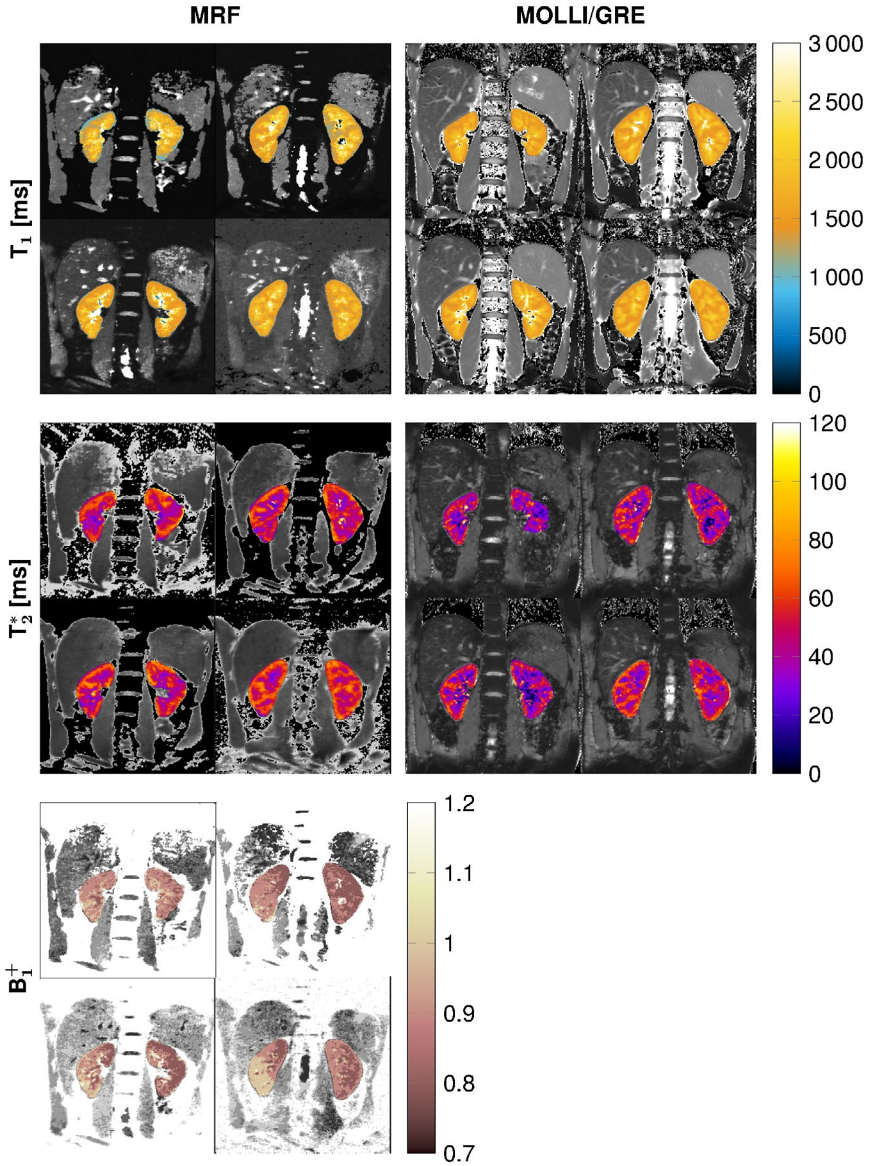

FIGURE 5 Exemplary baselines image, T_1, T_2^*, and B_1^+ maps for 4 slice of the MRF, MOLLI, and multi-GRE in the kidneys in coronal view

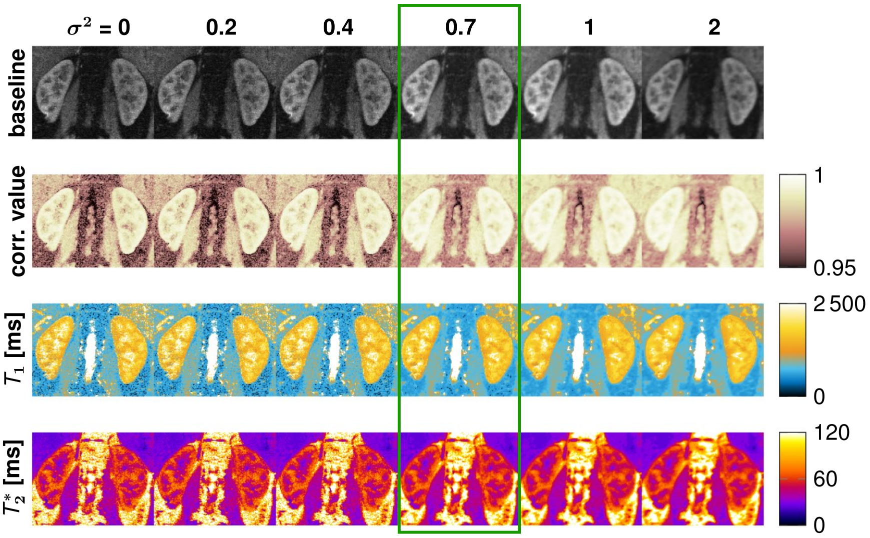

FIGURE 6 Top panel shows the baseline images with different variances of the Gaussian filter with a kernel size equal to 5. Correlation maps depict the matrix multiplication of the matching process which should be equal to 1 for a perfect match. T_1 and T_2^* maps are depicted to visualize the effect for different variances on the baseline images

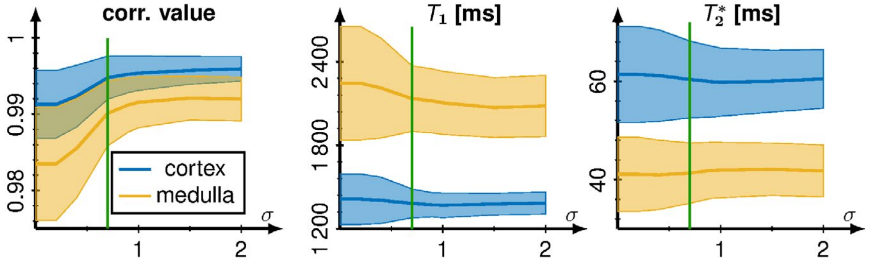

FIGURE 7 The correlation values, T_1 and T_2^* times are illustrated for the cortex (blue) and the medulla (yellow) for increasing variance. The shaded area depicts the corresponding standard deviation. The green lines mark the chosen noise setting

slightly overestimated T_1 and T_2^* times and higher standard deviations than MOLLI. T_2^* map quality was similar to multi-GRE. T_1 times showed larger intersubject variation and medulla T_1 MOLLI and MRF values were higher than in the literature.[11,15]

Quantitative diagnosis requires a clear separation of diseased and healthy kidneys. Sensitivity is thus determined by the underlying pathological alteration and the precision of the measurement technique. Major variations are observed in diseased kidneys (CKD) by increased T_1 times of over 150 ms (10%) in the cortex, but just around 50 ms (5%) in the medulla and increased T_2^* times of around 3-5 ms (10%) in the medulla and cortex.[15] Therefore, with the precision of the MRF parametric maps of around 30 ms for T_1 and less than 2 ms of T_2^*, we assume that it is possible to identify pathological changes induced by CKD with our proposed method.

We based our sequence of the EPI-MRF as fully sampled baseline images which is beneficial in clinical routines. This and the fast group match reconstruction in-line on the scanner enables the possibility to change imaging parameters such as the FOV during the clinical workflow based on patient size and position to overcome ghosting artifacts. Compared to conventional MRF methods using unbalanced SSFP sequences, our MRF method was resilient to banding artifacts and incomplete gradient refocusing.[34,35] However, rapid acquisitions require a trade-off against noise resilience. Therefore, we analyzed the impact of Gaussian filtering on the baseline images. This improved the image quality of the T_1 and T_2^* maps and reduced the standard deviation without changing the mean value. The correlation value of every pixel was increased meaning that the matching process is more accurate.

MRF EPI has the drawback of potential motion during the readout, therefore complete baseline images can be used easily for motion correction in post-processing. Slice tracking based on navigators can be used to port the method to free-breathing and is subject of future research.

The image quality of the MRF parameter maps is highly dependent on the image quality of the baseline images. Therefore, improving the EPI baseline image quality was shown to improve the MRF map quality. Reduction of ghosting artifacts,[36,37] Nyquist artifact,[38,39] and motion correction[40] were recently published, which all have the potential to improve the image quality of the proposed MRF method. Despite advanced shimming, field inhomogeneities disturb the k-space echo train and therefore lead to geometric distortions.[41,42] Gain in SNR could be achieved by using a 3D EPI readout when imaging with high resolution at the cost of increasing minimal TE.[43,44] Novel MRF reconstruction methods including deep learning can be used for accelerating the reconstruction and obtain more stable matching progress.[45-49] Optimizing the pulse sequence by a better choice of the flip angle, TE, and TR may further decrease the noise as published recently.[50]

This study has some limitations. Despite the nominally high spatial resolution, the effective resolution is lower due to the use of Gaussian filtering. The Siemens scanner treats the missing k-space lines by zero filling. Additionally, without using 5/8 partial Fourier, the maps are worse due to the longer TE. For this kidney MRF sequence, it was essential to push the TE as short as possible to overcome blurring. However, 5/8 partial Fourier reduces the lines in k-space and therefore further widens the point spread function. Susceptibility artifacts due to the air in the lung disturb the parametric MRF maps compared to the reference methods, which is widely known as EPI distortion. Therefore, distortion correction may improve the image quality.[51,52]

A small number of volunteers were measured with relatively low fat content and all young in age. Higher fat content and incorrect breath-hold will significantly reduce the SNR. Larger cohorts in different age groups and patients with CKD or kidney transplants are needed to further evaluate the proposed sequence and to implement the kidney MRF in the clinical routine.

5 | CONCLUSIONS

In this study, we have shown the feasibility of an EPI-MRF sequence for simultaneous quantification of T_1 and T_2^* in the kidneys during a single breath-hold using 4 slices. Using single shot imaging and in-line reconstruction on the scanner system enables to monitor the baseline images while scanning to correct for patient specific artifacts in clinical work flow.

ORCID

Ingo Hermann http://orcid.org/0000-0002-6379-5299
Jorge Chacon-Caldera http://orcid.org/0000-0002-0529-1826
Sebastian Weingärtner http://orcid.org/0000-0002-0739-6306

REFERENCES

1. Ma D, Gulani V, Seiberlich N, et al. Magnetic resonance fingerprinting. *Nature*. 2013;495:187–192.
2. Rieger B, Zimmer F, Zapp J, Weingärtner S, Schad LR. Magnetic resonance fingerprinting using echo-planar imaging: joint quantification of T_1 and relaxation times. *Magn Reson Med*. 2017;78:1724–1733.
3. Khajehim M, Christen T, Chen JJ. Magnetic resonance fingerprinting with combined gradient- and spin-echo echo-planar imaging: simultaneous estimation of T_1, T_2 and T_2* with integrated-B_1 correction. *bioRxiv*. 2019:604546. http://dx.doi.org/info:doi/10.1101/604546.
4. Wang CY, Coppo S, Mehta BB, Seiberlich N, Yu X, Griswold MA. Magnetic resonance fingerprinting with quadratic RF phase for measurement of T_2* simultaneously with δf, T_1, and T_2. *Magn Reson Med*. 2019;81:1849–1862.
5. Wyatt CR, Smith TB, Sammi MK, Rooney WD, Guimaraes AR. Multi-parametric T_2* magnetic resonance fingerprinting using variable echo times. *NMR Biomed*. 2018;31:e3951.
6. Hamilton JI, Jiang Y, Chen Y, et al. MR fingerprinting for rapid quantification of myocardial T_1, T_2, and proton spin density. *Magn Reson Med*. 2017;77:1446–1458.
7. Panda A, Mehta BB, Coppo S, et al. Magnetic resonance fingerprinting—an overview. *Curr Opin Biomed Eng*. 2017; 3:56–66.
8. Rieger B, Akçakaya M, Pariente JC, et al. Time efficient whole-brain coverage with MR fingerprinting using slice-interleaved echo-planar-imaging. *Sci Rep*. 2018;8:2045–2322.
9. Hermann I, Rieger B, Zapp J, Weingärtner S, Schad LR. Optimized fast dictionary matching for magnetic resonance fingerprinting based on echo-planar imaging for enhanced clinical workflow. Proceedings from the 27th Annual Meeting ISMRM, Montreal, QC, Canada. 2019:4529.
10. Chen Y, Jiang Y, Pahwa S, et al. MR fingerprinting for rapid quantitative abdominal imaging. *Radiology*. 2016;279:278–286.
11. Wolf M, Boer A, Sharma K, et al. Magnetic resonance imaging T_1- and T_2-mapping to assess renal structure and function: a systematic review and statement paper. *Nephrol Dial Transplant*. 2018;33:ii41–ii50.
12. Schley G, Jordan J, Ellmann S, et al. Multiparametric magnetic resonance imaging of experimental chronic kidney disease: a quantitative correlation study with histology. *PLOS ONE*. 2018;13:1–18.
13. Thurman J, Gueler F. Recent advances in renal imaging. *F1000 Res*. 2018;7:278–286.
14. Villa G, Ringgaard S, Hermann I, et al. Phase-contrast magnetic resonance imaging to assess renal perfusion: a systematic review and statement paper. *MAGMA*. 2019;1–19. http://dx.doi.org/info:doi/10.1007/s10334-019-00772-0.
15. Cox EF, Buchanan CE, Bradley CR, et al. Multiparametric renal magnetic resonance imaging: validation, interventions, and alterations in chronic kidney disease. *Front Physiol*. 2017;8. Abstract 696.
16. Milani B, Ansaloni A, Sousa-Guimaraes S, et al. Reduction of cortical oxygenation in chronic kidney disease: evidence obtained with a new analysis method of blood oxygenation level-dependent magnetic resonance imaging. *Nephrol Dial Transplant*. 2016;32: 2097–2105.
17. Burnier M, Pruijm M, Mendichovszky IA, et al. Renal blood oxygenation level-dependent magnetic resonance imaging to measure renal tissue oxygenation: a statement paper and systematic review. *Nephrol Dial Transplant*. 2018;33:ii22–ii28.
18. Hedgire SS, McDermott S, Wojtkiewicz GR, Abtahi SM, Harisinghani M, Gaglia JL. Evaluation of renal quantitative T_2* changes on MRI following administration of ferumoxytol as a T_2* contrast agent. *Int J Nanomed*. 2014;9:2101–2207.
19. Nissen JC, Mie MB, Zöllner FG, Haneder S, Schoenberg SO, Michaely HJ. Blood oxygenation level dependent (BOLD)—Bildgebung der Nieren: Konzepte und Anwendungen. *Z Med Phys*. 2010;20:88–100.
20. Look DC, Locker DR. Time saving in measurement of NMR and EPR relaxation times. *Rev Sci Instrum*. 1970;41:250–251.
21. Messroghli DR, Radjenovic A, Kozerke S, Higgins DM, Sivananthan MU, Ridgway JP. Modified Look-Locker inversion recovery (MOLLI) for high-resolution T_1 mapping of the heart. *Magn Reson Med*. 2004;52:141–146.
22. Radenkovic D, Weingärtner S, Ricketts L, Moon JC, Captur G. T_1 mapping in cardiac MRI. *Heart Failure Rev*. 2017;22:415–430.
23. Pedersen M, Dissing TH, Merkenborg JAN, et al. Validation of quantitative BOLD MRI measurements in kidney: application to unilateral ureteral obstruction. *Kidney Int*. 2005;67:2305–2312.
24. Thacker JM, Li L-P, Li W, Zhou Y, Sprague SM, Prasad PV. Reduction of cortical oxygenation in chronic kidney disease: evidence obtained with a new analysis method of blood oxygenation level-dependent magnetic resonance imaging. *Nephrol Dial Transplant*. 2015;50:821–827.
25. Pruijm M, Mendichovszky IA, Liss P, et al. Renal blood oxygenation level-dependent magnetic resonance imaging to measure renal tissue oxygenation: a statement paper and systematic review. *Nephrol Dial Transplant*. 2018;33:ii22–ii28.
26. Ding Y, Mason RP, McColl RW, et al. Simultaneous measurement of tissue oxygen level-dependent (TOLD) and blood oxygenation level-dependent (BOLD) effects in abdominal tissue oxygenation level studies. *J Magn Reason*. 2013;38:1230–1236.
27. Kellman P, Hansen MS. T_1-mapping in the heart: accuracy and precision. *Magn Reson Med*. 2014;16:2.
28. Panek R, Welsh L, Dunlop A, et al. Repeatability and sensitivity of measurements in patients with head and neck squamous cell carcinoma at 3T. *J Magn Reason*. 2016;44:72–80.
29. Kellman P, Wilson JR, Xue H, Ugander M, Arai AE. Extracellular volume fraction mapping in the myocardium, part 1: evaluation of an automated method. *J Cardiovasc Magn Reason*. 2012;14. Abstract 63.
30. Cauley SF, Setsompop K, Ma D, et al. Fast group matching for MR fingerprinting reconstruction. *Magn Reson Med*. 2015;74:523–528.
31. Captur G, Gatehouse P, Keenan KE, et al. A medical device-grade T_1 and ECV phantom for global T_1 mapping quality assurance—the T_1 Mapping and ECV Standardization in cardiovascular magnetic resonance (T_1MES) program. *J Cardiovasc Magn Reason*. 2016;18. Abstract 58.

32. Chen N-K, Wyrwicz AM. Correction for EPI distortions using multi-echo gradient-echo imaging. *Magn Reson Med*. 1999;41:1206–1213.
33. Tsao J. Ultrafast imaging: principles, pitfalls, solutions, and applications. *J Magn Reason*. 2010;32:252–266.
34. Jiang Y, Ma D, Seiberlich N, Gulani V, Griswold MA. MR fingerprinting using fast imaging with steady state precession (FISP) with spiral readout. *Magn Reson Med*. 2015;74:1621–1631.
35. Barmet C, Zanche ND, Pruessmann KP. Spatiotemporal magnetic field monitoring for MR. *Magn Reson Med*. 2008;60:187–197.
36. Ianni JD, Welch EB, Grissom WA. Ghost reduction in echo-planar imaging by joint reconstruction of images and line-to-line delays and phase errors. *Magn Reson Med*. 2018;79:3114–3121.
37. Kim Y-C, Nielsen J-F, Nayak KS. Automatic correction of echo-planar imaging (EPI) ghosting artifacts in real-time interactive cardiac MRI using sensitivity encoding. *J Magn Reason*. 2008;27:239–245.
38. Chang H-C, Chen N-K. Joint correction of Nyquist artifact and minuscule motion-induced aliasing artifact in interleaved diffusion weighted EPI data using a composite two-dimensional phase correction procedure. *Mag Reson Imaging*. 2016;34:974–979.
39. Xie VB, Lyu M, Liu Y, Feng Y, Wu EX. Robust EPI Nyquist ghost removal by incorporating phase error correction with sensitivity encoding (PEC-SENSE). *Magn Reson Med*. 2018;79:943–951.
40. Dong Z, Wang F, Ma X, Dai E, Zhang Z, Guo H. Motion-corrected k-space reconstruction for interleaved EPI diffusion imaging. *Magn Reson Med*. 2018;79:1992–2002.
41. Finsterbusch J. Chapter 2.2—B_0 inhomogeneity and shimming. In: Cohen-Adad J, Wheeler-Kingshott CAM, eds. *Quantitative MRI of the Spinal Cord*. San Diego: Academic Press, 2014:68–90.
42. Saritas EU, Holdsworth SJ, Bammer R. Chapter 2.3—susceptibility artifacts. In: Cohen-Adad J, Wheeler-Kingshott CAM, eds. *Quantitative MRI of the Spinal Cord*. San Diego: Academic Press, 2014:91–105.
43. Hu Y, Glover GH. Three-dimensional spiral technique for high-resolution functional MRI. *Magn Reson Med*. 2007;58:947–951.
44. Todd N, Josephs O, Callaghan MF, Lutti A, Weiskopf N. Prospective motion correction of 3D echo-planar imaging data for functional MRI using optical tracking. *NeuroImage*. 2015;113:1–12.
45. Hoppe E, Körzdörfer G, Würfl T, et al. Deep learning for magnetic resonance fingerprinting: a new approach for predicting quantitative parameter values from time series. *Stud Health Technol Inform*. 2017;243:202–206.
46. Cohen O, Zhu B, Rosen MS. Deep learning for rapid sparse MR fingerprinting reconstruction. *CoRR*. 2017. https://arxiv.org/abs/1710.05267. Accessed January 1, 2020.
47. Lundervold AS, Lundervold A. An overview of deep learning in medical imaging focusing on MRI. *Z Med Phys*. 2019;29:102–127.
48. Maier A, Syben C, Lasser T, Riess C. A gentle introduction to deep learning in medical image processing. *Z Med Phys*. 2019;29:96–101.
49. Schnurr A, Chung K, Russ T, Schad LR, Zöllner FG. Simulation-based deep artifact correction with Convolutional Neural Networks for limited angle artifacts. *Z Med Phys*. 2019;29:150–161.
50. Lee PK, Watkins LE, Anderson TI, Buonincontri G, Hargreaves BA. Flexible and efficient optimization of quantitative sequences using automatic differentiation of Bloch simulations. *Magn Reson Med*. 2019;82:1438–1451.
51. In M-H, Speck O. Highly accelerated PSF-mapping for EPI distortion correction with improved fidelity. *MAGMA*. 2012;25:183–192.
52. Hong X, To XV, Teh I, Soh JR, Chuang K-H. Evaluation of EPI distortion correction methods for quantitative MRI of the brain at high magnetic field. *Magn Reson Imaging*. 2015;33:1098–1105.

How to cite this article: Hermann I, Chacon-Caldera J, Brumer I, et al. Magnetic resonance fingerprinting for simultaneous renal T_1 and T_2^* mapping in a single breath-hold. *Magn Reson Med*. 2020;00:1–9. https://doi.org/10.1002/mrm.28160